The Astrophysical Journal, 944:148 (11pp), 2023 February 20 https://doi.org/10.3847/1538-4357/acb25a

Quantifying the Agyrotropy of Proton and Electron Heating in Turbulent Plasmas

Yan Yang[1], Francesco Pecora[1], William H. Matthaeus[1], Sohom Roy[1], Manuel Enrique Cuesta[1], Alexandros Chasapis[2], Tulasi Parashar[3], Riddhi Bandyopadhyay[4], D. J. Gershman[5], B. L. Giles[5], and J. L. Burch[6]
[1] Department of Physics and Astronomy, University of Delaware, Newark, DE, 19716, USA
[2] Laboratory for Atmospheric and Space Physics, University of Colorado Boulder, Boulder, CO, 80309, USA
[3] School of Chemical and Physical Sciences, Victoria University of Wellington, Wellington 6012, New Zealand
[4] Department of Astrophysical Sciences, Princeton University, Princeton, NJ, 08544, USA
[5] NASA Goddard Space Flight Center, Greenbelt, MD, 20771, USA
[6] Southwest Research Institute, San Antonio, TX, 78238, USA
Received 2022 October 21; revised 2023 January 5; accepted 2023 January 10; published 2023 February 21

Abstract

An important aspect of energy dissipation in weakly collisional plasmas is that of energy partitioning between different species (e.g., protons and electrons) and between different energy channels. Here we analyse pressure–strain interaction to quantify the fractions of isotropic compressive, gyrotropic, and nongyrotropic heating for each species. An analysis of kinetic turbulence simulations is compared and contrasted with corresponding observational results from Magnetospheric Multiscale Mission data in the magnetosheath. In assessing how protons and electrons respond to different ingredients of the pressure–strain interaction, we find that compressive heating is stronger than incompressive heating in the magnetosheath for both electrons and protons, while incompressive heating is stronger in kinetic plasma turbulence simulations. Concerning incompressive heating, the gyrotropic contribution for electrons is dominant over the nongyrotropic contribution, while for protons nongyrotropic heating is enhanced in both simulations and observations. Variations with plasma β are also discussed, and protons tend to gain more heating with increasing β.

Unified Astronomy Thesaurus concepts: Space plasmas (1544); Plasma physics (2089); Interplanetary turbulence (830); Interplanetary physics (827); Planetary magnetospheres (997)

1. Introduction

Electrons and ions, having disparate masses, can be energized by distinct mechanisms in plasmas. There is ample evidence that supports differential heating for ions and electrons. For example, the findings of Cranmer (2009) and Hughes et al. (2014) favor stronger ion heating, while Bandyopadhyay et al. (2021) and Yang et al. (2022) report stronger electron heating. As suggested in early studies, the partitioning of heating between ions and electrons could depend on the turbulence amplitude (Stawarz et al. 2009; Wu et al. 2013; Matthaeus et al. 2016; Hughes et al. 2017; Roy et al. 2022) and plasma β (the ratio of thermal to magnetic pressure) (Quataert 1998; Howes 2010; Klein et al. 2017; Parashar et al. 2018; Vech et al. 2017; Kawazura et al. 2019; Schekochihin et al. 2019). To quantify the distribution of energy between species, there is an increasing awareness that the pressure–strain interaction (Yang et al. 2017a, 2017b, 2019; Pezzi et al. 2019; Hunana et al. 2019; Matthaeus et al. 2020; Lapenta et al. 2020; Yang et al. 2022; Hellinger et al. 2022) is a direct way to identify incompressive versus compressive heating (Chasapis et al. 2018; Du et al. 2018; Pezzi et al. 2020; Wang et al. 2021; Zhou et al. 2021; Bandyopadhyay et al. 2021), as well as ion versus electron heating (Sitnov et al. 2018; Bandyopadhyay et al. 2021; Roy et al. 2022). Recently, species-dependent pressure–strain has been employed in quantifying how an initial Alfvén wave degenerates due to a phase-mixing process (Bacchini et al. 2022) and in magnetic reconnection (Fadanelli et al. 2021; Barbhuiya & Cassak 2022; Rueda et al. 2022).

The pressure tensor is the velocity space average of the stresses resulting from all guiding center drifts and finite Larmor radius (FLR) effects, and comprises six independent components. It is frequently deemed to be isotropic in the framework of magnetohydrodynamic (MHD) modeling, or gyrotropic, i.e., cylindrically symmetric about the magnetic field, as it is in the double-adiabatic or Chew–Goldberger–Low (CGL) closures (Chew et al. 1956). In magnetized plasmas, fast particle gyromotion in a strong magnetic field tends to render the pressure tensor isotropic in the plane perpendicular to the magnetic field. Thus a strong magnetic field, in the absence of other effects, promotes gyrotropy. However, deviation from gyrotropy, i.e., agyrotropy, is not negligible when the characteristic length scales of the plasma are comparable to the particle gyroradius, or alternatively the timescales become comparable with the gyro period. In this sense, electrons are likely to be well-modeled as gyrotropic since the small mass of electrons implies the necessity of very small spatial or timescales for gyrotropy violation. However, both numerical and observational evidence have been presented that nongyrotropic electron pressure tensors can break the "frozen-in" condition to enable collisionless magnetic reconnection to occur in current layers approaching the scale of the thermal electron gyroradius (Vasyliunas 1975; Hesse et al. 1999, 2002; Pritchett 2001; Ricci et al. 2004; Scudder & Daughton 2008; Scudder et al. 2012, 2015; Cassak et al. 2015; Burch et al. 2016; Graham et al. 2017). Meanwhile, one can anticipate that it is much easier for the vastly more massive ions to induce nongyrotropic pressure tensors (Servidio et al. 2015). This issue is intimately related to the occurrence of the non-Maxwellian feature of ion distribution functions and enhanced

kinetic effects, often associated with magnetic, density, and velocity gradients (Servidio et al. 2012, 2014; Valentini et al. 2014; He et al. 2015; Perri et al. 2020).

Concerning agyrotropy of the pressure tensor, it is possible to identify certain conditions under which the off-diagonal components of the pressure tensor can be related to lower-order moments. Closure models for the pressure tensor date back to Chapman & Cowling (1939) and Marshall (1960), where a first-order term is introduced as a small correction or perturbation to the Maxwellian distribution function. The off-diagonal pressure tensor is proportional to a coefficient of viscosity (Landshoff 1949; Spitzer & Härm 1953; Braginskii 1965) and a velocity gradient (Kaufman 1960; Thompson 1961; Roberts & Taylor 1962; Braginskii 1965), an approximation of great practical importance. For example, a FLR correction is introduced to the ion pressure tensor (Yajima 1966; Khanna & Rajaram 1982; Smolyakov 1998; Cerri et al. 2013, 2014; De Camillis et al. 2016), which captures the physics approaching the ion gyroradius (or the ion inertial length). However, this closure applies only when macroscopic quantities vary slowly in space and time with respect to the collision mean free path[7] and the collision time. Then, the local distribution relaxes to a Maxwellian in a time of the order of the collision time (Braginskii 1965). This requirement is rarely satisfied in space plasma turbulence, in which coherent structures like current sheets can steepen to electron scales, leading to anisotropic electron and ion distributions (Karimabadi et al. 2013). Without resorting to this viscous model, Del Sarto et al. (2016) and Del Sarto & Pegoraro (2018) proceed with the pressure tensor evolution equation retaining full pressure tensor dynamics, which remains viable even when collisional relaxation to Maxwellian is either absent or slow. They found that even in an almost collisionless system, the shear flow and the pressure tensor anisotropy are strongly coupled and interact on fast timescales.

The nongyrotropic-to-gyrotropic heating of the pressure–strain interaction for ions and electrons had already been discussed briefly by Du et al. (2018) and Bacchini et al. (2022) in 2D kinetic simulations. The suggestion is that the dominant contributions for ions and electrons are nongyrotropic and gyrotropic, respectively. Here a more systematic study is presented emphasizing the nongyrotropic-to-gyrotropic heating of each species with varying plasma β. Both kinetic particle-in-cell (PIC) simulations and the Magnetospheric Multiscale Mission (MMS) observational data in the Earth's magnetosheath are employed.

2. Decomposition of Pressure Work

In the classical turbulence cascade scenario, energy is transferred across scales, and is ultimately dissipated, adding to the thermal energy reservoir. Quantities frequently invoked to describe energy conversion include the rate of work done by the electric field on particles for species α, $\boldsymbol{j}_\alpha\cdot\boldsymbol{E}$ (Zenitani et al. 2011), and the pressure–strain interaction for species α, $-(\boldsymbol{P}_\alpha\cdot\nabla)\cdot\boldsymbol{u}_\alpha$ (Yang et al. 2017a, 2017b). One can readily see the different roles of the two pathways from energy balance equations. The hierarchy of the moments of the Vlasov–Maxwell equations yields the time evolution of the electromagnetic $E^m=(\boldsymbol{B}^2+\boldsymbol{E}^2)/(8\pi)$, bulk flow kinetic $E_\alpha^f=\rho_\alpha\boldsymbol{u}_\alpha^2/2$, and internal or thermal $E_\alpha^{\rm th}=\frac{1}{2}m_\alpha\int(\boldsymbol{v}-\boldsymbol{u}_\alpha)^2 f_\alpha(\boldsymbol{x},\boldsymbol{v},t)d\boldsymbol{v}$ energies:

$$\partial_t E_\alpha^f+\nabla\cdot(E_\alpha^f\boldsymbol{u}_\alpha+\boldsymbol{P}_\alpha\cdot\boldsymbol{u}_\alpha)=(\boldsymbol{P}_\alpha\cdot\nabla)\cdot\boldsymbol{u}_\alpha+\boldsymbol{j}_\alpha\cdot\boldsymbol{E}, \quad (1)$$

$$\partial_t E_\alpha^{\rm th}+\nabla\cdot(E_\alpha^{\rm th}\boldsymbol{u}_\alpha+\boldsymbol{h}_\alpha)=-(\boldsymbol{P}_\alpha\cdot\nabla)\cdot\boldsymbol{u}_\alpha \quad (2)$$

,

$$\partial_t E^m+\frac{c}{4\pi}\nabla\cdot(\boldsymbol{E}\times\boldsymbol{B})=-\boldsymbol{j}\cdot\boldsymbol{E}, \quad (3)$$

where $\boldsymbol{P}_\alpha$ is the pressure tensor, $\boldsymbol{h}_\alpha$ is the heat flux vector, $\boldsymbol{j}=\sum_\alpha\boldsymbol{j}_\alpha$ is the total electric current density, $\boldsymbol{j}_\alpha=n_\alpha q_\alpha\boldsymbol{u}_\alpha$ is the electric current density of species α, and n_α and q_α are the number density and the charge of species α, respectively. Note that the divergence terms (i.e., the second terms on the left-hand side) transport energy spatially without changing the form of the energy. The electric work, $\boldsymbol{j}_\alpha\cdot\boldsymbol{E}$, exchanges electromagnetic energy with fluid flow energy for species α, while the pressure–strain interaction, $-(\boldsymbol{P}_\alpha\cdot\nabla)\cdot\boldsymbol{u}_\alpha$, converts fluid flow energy into thermal energy for species α.

There might be several definitions of "heating". Here by "heating", we refer to the reduction of energy in the electromagnetic fields and in the fluid velocity fluctuations, which is converted into the random kinetic energy of particles (which is called internal or thermal energy $E_\alpha^{\rm th}$ in this paper). This leads to an increase of particle temperature. We focus on the pressure–strain interaction since it determines the rate of the local conversion of energy into thermal energy (Pezzi et al. 2019; Bacchini et al. 2022; Yang et al. 2022). The pressure–strain interaction is further capable of differentiating effects on electrons and protons (and additional species if present), as well as distinguishing incompressive and compressive heating, isotropic and anisotropic heating, and local and global heating. Alternate decompositions of the pressure–strain interaction (Cassak & Barbhuiya 2022; Cassak et al. 2022) have been investigated for interpreting the underlying physics in the energy-conversion process.

The pressure tensor of the α species can be decomposed into isotropic, gyrotropic, and nongyrotropic parts as follows:

$$\boldsymbol{P}_\alpha=p_\alpha\boldsymbol{I}+\underbrace{(p_{\parallel,\alpha}-p_{\perp,\alpha})\left(\boldsymbol{bb}-\frac{1}{3}\boldsymbol{I}\right)}_{\boldsymbol{P}_{g,\alpha}}+\boldsymbol{P}_{ng,\alpha}, \quad (4)$$

where $\boldsymbol{I}$ is the identity tensor, $p_\alpha=\mathrm{Tr}(\boldsymbol{P}_\alpha)/3=(P_{xx,\alpha}+P_{yy,\alpha}+P_{zz,\alpha})/3$ is the scalar pressure, $\boldsymbol{P}_{g,\alpha}$ and $\boldsymbol{P}_{ng,\alpha}$ are the gyrotropic and nongyrotropic parts of the pressure tensor, respectively, $\boldsymbol{b}=\boldsymbol{B}/|\boldsymbol{B}|$ is a unit vector along the local magnetic field, and $p_{\parallel,\alpha}=\boldsymbol{b}\cdot\boldsymbol{P}_\alpha\cdot\boldsymbol{b}$ and $p_{\perp,\alpha}=(\mathrm{Tr}(\boldsymbol{P}_\alpha)-p_{\parallel,\alpha})/2$ are the parallel and perpendicular pressure of the α species to the local magnetic field. The isotropic pressure p_α is discussed separately since it is combined with the compressive rate of velocity gradients directly, as shown below. The pressure–strain interaction is decomposed as:

$$-(\boldsymbol{P}_\alpha\cdot\underbrace{\nabla}_{\mathrm{PS}_e})\cdot\boldsymbol{u}_\alpha=-p_\alpha\underbrace{\nabla}_{p\theta_\alpha}\cdot\boldsymbol{u}_\alpha$$
$$-(p_{\parallel,\alpha}-\underbrace{p_{\perp,\alpha}}_{\mathrm{PiD}_{g,\alpha}})\boldsymbol{bb}:\boldsymbol{D}_\alpha-(\boldsymbol{P}_{ng,\alpha}\cdot\underbrace{\nabla}_{\mathrm{PiD}_{ng,\alpha}})\cdot\boldsymbol{u}_\alpha, \quad (5)$$

[7] In magnetized plasmas with a strong magnetic field, the LR could take the place of the usual mean free path.

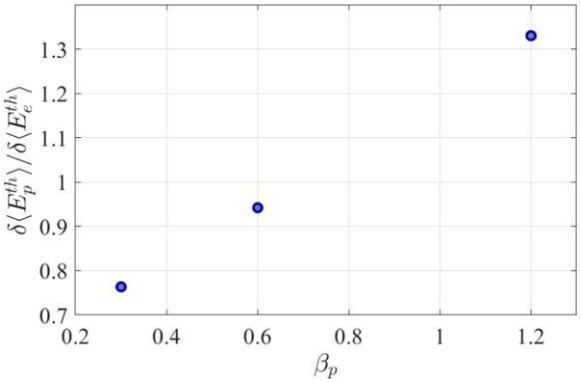

Figure 1. 2.5D PIC: the ratio between electron and proton thermal energy increase at different βs. The change of energy is defined as $\delta E = E(t = 298\omega_{ci}^{-1}) - E(t = 9\omega_{ci}^{-1})$.

where $D_{ij,\alpha} = (\partial_i u_{j,\alpha} + \partial_j u_{i,\alpha})/2 - (\nabla \cdot \boldsymbol{u}_\alpha)\delta_{ij}/3$ is the traceless symmetric part of the strain tensor and $p\theta_\alpha$, $\mathrm{PiD}_{g,\alpha}$ and $\mathrm{PiD}_{ng,\alpha}$ denote the compressive, gyrotropic, and nongyrotropic parts, respectively (Du et al. 2018; Cassak et al. 2022). Obviously, the incompressive part is $\mathrm{PiD}_\alpha = \mathrm{PiD}_{g,\alpha} + \mathrm{PiD}_{ng,\alpha}$.

3. Kinetic Simulation Results

To quantify the contribution of incompressive PiD_α versus compressive $p\theta_\alpha$ and gyrotropic $\mathrm{PiD}_{g,\alpha}$ versus the nongyrotropic $\mathrm{PiD}_{ng,\alpha}$ conversion of energy through the pressure–strain interaction and its plasma β dependence, we begin with fully kinetic PIC simulations of a fully ionized proton–electron plasma with varying β.

Undriven kinetic PIC simulations employing the code P3D (Zeiler et al. 2002) were implemented in a periodic 2.5D geometry (three vector components but no variation in the z direction). Large-scale fluctuations were initialized in a square domain of size $L \simeq 150\, d_i$, where d_i is the ion inertial length. There are 4096^2 grid points and 3200 particles of each species per cell ($\sim 1.07 \times 10^{11}$ total particles). For numerical reasons, the ion-to-electron mass ratio is chosen to be $m_i/m_e = 25$, and the ratio $\omega_{\mathrm{pe}}/\omega_{ce} = 3$ (where ω_{pe} is the electron plasma frequency and ω_{ce} is the electron cyclotron frequency). All simulations have the same initial conditions except that the plasma β is varied by adjusting the initial proton and electron temperatures. The initial density is uniform and protons and electrons are Maxwellian-distributed with equal initial temperatures. An out-of-plane magnetic field $B_0 = 1.0$ is applied, and $\beta_e = \beta_i = 0.3,\ 0.6,\ 1.2$. The transverse velocity and magnetic perturbations were seeded at time $t = 0$ at wavenumbers $2 \leqslant |\boldsymbol{k}| \leqslant 4$ with random phased fluctuations and a specific spectrum. Each run was evolved for more than $300\omega_{ci}^{-1}$. These simulations were also used by et al. (2018), Yang et al. (2019), Matthaeus et al. (2020), Bandyopadhyay et al. (2021), Adhikari et al. (2021), Yang et al. (2022), and Roy et al. (2022).

As a first step, we examine the time evolution of the thermal energy density of each species $\langle E_\alpha^{\mathrm{th}}\rangle$ and the rate of temperature increase for each species. The latter is quantified by tabulating the total thermal energy density increase $\delta\langle E_\alpha^{\mathrm{th}}\rangle$ over the time period $[9,\ 298](\omega_{ci}^{-1})$. Here the brackets $\langle\cdots\rangle$ denote the spatial average over the whole domain. We avoid the early time interval over which the system experiences rapid adjustments associated with the prescribed initial conditions in accord with the Vlasov–Maxwell equation (this is a standard feature of PIC codes.) Figure 1 shows the ratio $\delta\langle E_p^{\mathrm{th}}\rangle/\delta\langle E_e^{\mathrm{th}}\rangle$. It is evident that with increasing β, the protons gain more thermal energy. Therefore a larger β favors proton heating relative to electron heating, which is consistent with Parashar et al. (2018).

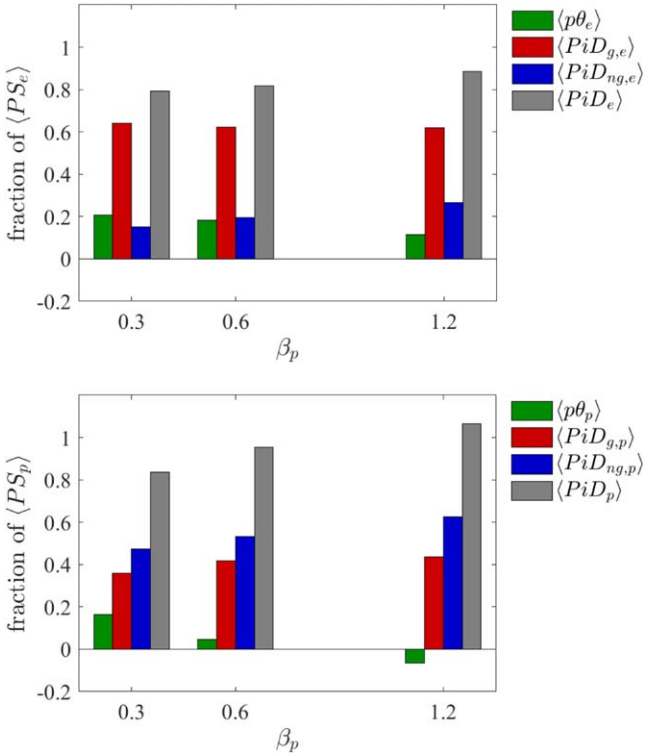

Figure 2. 2.5D PIC: percentages of the cumulatively time-integrated compressive $\langle p\theta_\alpha\rangle$, incompressive $\langle \mathrm{PiD}_\alpha\rangle$, gyrotropic $\langle \mathrm{PiD}_{g,\alpha}\rangle$, and nongyrotropic $\langle \mathrm{PiD}_{ng,\alpha}\rangle$ contributions relative to the pressure–strain interaction $\langle \mathrm{PS}_\alpha\rangle$ for electrons and protons at different βs. The cumulative integral is computed over time $[9,\ 298]$ in units of ω_{ci}^{-1}.

As shown by Pezzi et al. (2019), Yang et al. (2022), Bacchini et al. (2022), and Roy et al. (2022), the pressure–strain interaction is an exact representation of energy conversion into thermal energy. It is useful to tally the fraction of total heating due to each ingredient of the pressure–strain interaction during the fully integrated time period. Using the same series of kinetic PIC simulations described above, the different contributions to the pressure–strain interaction are cumulatively time-integrated through the trapezoidal rule over the same time interval $[9,\ 298](\omega_{ci}^{-1})$. For several simulations of varying β, Figure 2 shows the percentage contributions to the total pressure–strain interaction $\langle \mathrm{PS}_\alpha\rangle$ for electrons and protons, from the compressive $\langle p\theta_\alpha\rangle$ ingredient, the gyrotropic $\langle \mathrm{PiD}_{g,\alpha}\rangle$ ingredient, and the nongyrotropic $\langle \mathrm{PiD}_{ng,\alpha}\rangle$ ingredient. Note that the incompressive contribution $\langle \mathrm{PiD}_\alpha\rangle$ is composed of gyrotropic and nongyrotropic contributions.

It is obvious that the spatially averaged incompressive part dominates over the spatially averaged compressive part for both electrons and ions. However, the electrons and ions exhibit notable disparities with respect to agyrotropy. The gyrotropic part is significantly stronger than the nongyrotropic part for electrons, while for protons the nongyrotropic part is elevated and even slightly larger than the gyrotropic part. Also noteworthy is that the compressive percentage decreases for runs with increasing β, which could be attributed to stronger compressibility with low β. Note that the higher β runs have a lower Mach number since the perturbations in MHD scale

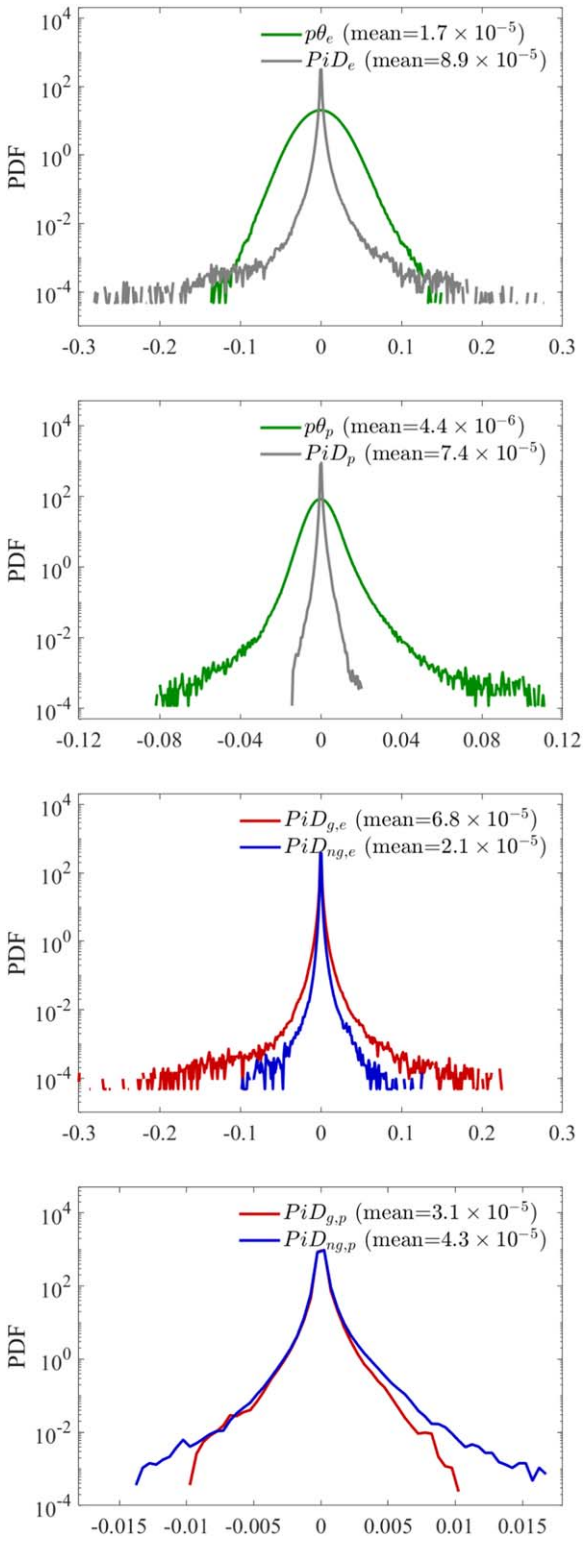

Figure 3. 2.5D PIC: PDFs of the incompressive and compressive parts and the gyrotropic and nongyrotropic parts of the pressure–strain interaction for electrons and protons at $\beta = 0.6$ and $t = 163\omega_{ci}^{-1}$. The variables listed are in units of $m_i n_0 v_A^3 d_i^{-1}$, where v_A is the Alfvén speed and n_0 is the reference value of number density.

velocity and magnetic field are identical in the three cases. The nongyrotropic contribution shows a slight increase with β.

A more detailed treatment of the components of the pressure–strain interaction is conducted by examining their pointwise values, spatial distributions, and probability distribution functions (PDFs) for both species, as illustrated in Figures 3 and 4. Here we only show the simulation with $\beta = 0.6$ at a time of $t = 163\omega_{ci}^{-1}$, shortly after the peak of the rms electric current density is reached and the turbulence is well developed. From Figure 4, one can see that the pointwise $p\theta_\alpha$ and PiD_α are not single-signed. A pointwise positive value means that the fluid kinetic energy is converted into thermal energy locally; conversely a pointwise negative value means the opposite direction of local energy conversion, i.e., flows driven by thermal forces. The PDFs of PiD_α exhibit significant departures from Gaussian distributions, with extended tails signifying intermittency, as can be seen clearly from the contour maps in Figure 4. However, a close inspection of $p\theta_\alpha$ reveals differences from PiD_α. First, although the spatially averaged compressive part is very small in Figure 2, its pointwise value could be larger than the incompressive part for both electrons and ions and the small spatial average results from the slightly skewed PDFs. Second, the central parts of the PDFs of $p\theta_\alpha$ are close to Gaussian distributions, which could correspond to the fine-scale positive and negative patches in Figure 4. The highly oscillating positive and negative values of $p\theta_\alpha$ may seem at first to be noise. But this also appears in our other simulations and in the MMS observational results shown in Section 4. This behavior could be associated with propagating waves, perhaps of an electrostatic nature. We will defer to a future study a more careful examination of these compressive features. We should note, however, that these oscillations are substantially eliminated by a scale filter (Yang et al. 2017a, 2022) or by a time average (Haggerty et al. 2017; Bandyopadhyay et al. 2021) procedure.

In Figure 4, the contour maps of the gyrotropic and nongyrotropic parts are very similar in their distributions in space, and both are reminiscent of the familiar nonuniformly distributed pattern of the intense electric current density (Wan et al. 2012; Karimabadi et al. 2013) typically seen in plasma turbulence. Consistent with the global behavior in Figure 2, for the electrons, the pointwise gyrotropic part $\mathrm{PiD}_{g,e}$ is much larger than the pointwise nongyrotropic part $\mathrm{PiD}_{ng,e}$; while the pointwise nongyrotropic part $\mathrm{PiD}_{ng,p}$ is slightly larger than the gyrotropic part $\mathrm{PiD}_{g,p}$ for the protons.

4. MMS Observation Results in the Magnetosheath

MMS includes four identical spacecraft, typically in a tetrahedral formation, and with small (∼10 km) separations. The MMS spacecraft sample the near-Earth plasma, including the magnetosheath (Burch et al. 2016). The proton and electron 3D velocity distribution functions (VDFs) are available from the Fast Plasma Investigation (FPI; Pollock et al. 2016) instrument. One can then determine both the pressure tensors and the velocity gradient tensors. The Flux-Gate Magnetometer (FGM; Russell et al. 2016) measures the vector magnetic field, used here for context.

To cover a wide range of plasma βs, we selected 30 intervals of MMS data in the magnetosheath, from 2016 January 11 to 2018 April 23; see Table 2. We used burst-mode measurements of the density, velocity, and the pressure tensor from the FPI instrument, with a time resolution of 150 ms for ions and 30 ms for electrons (Pollock et al. 2016). These intervals have relatively small elongation and planarity parameter values that characterize the quality of the MMS tetrahedron configuration. During these intervals MMS was in good tetrahedral formation,

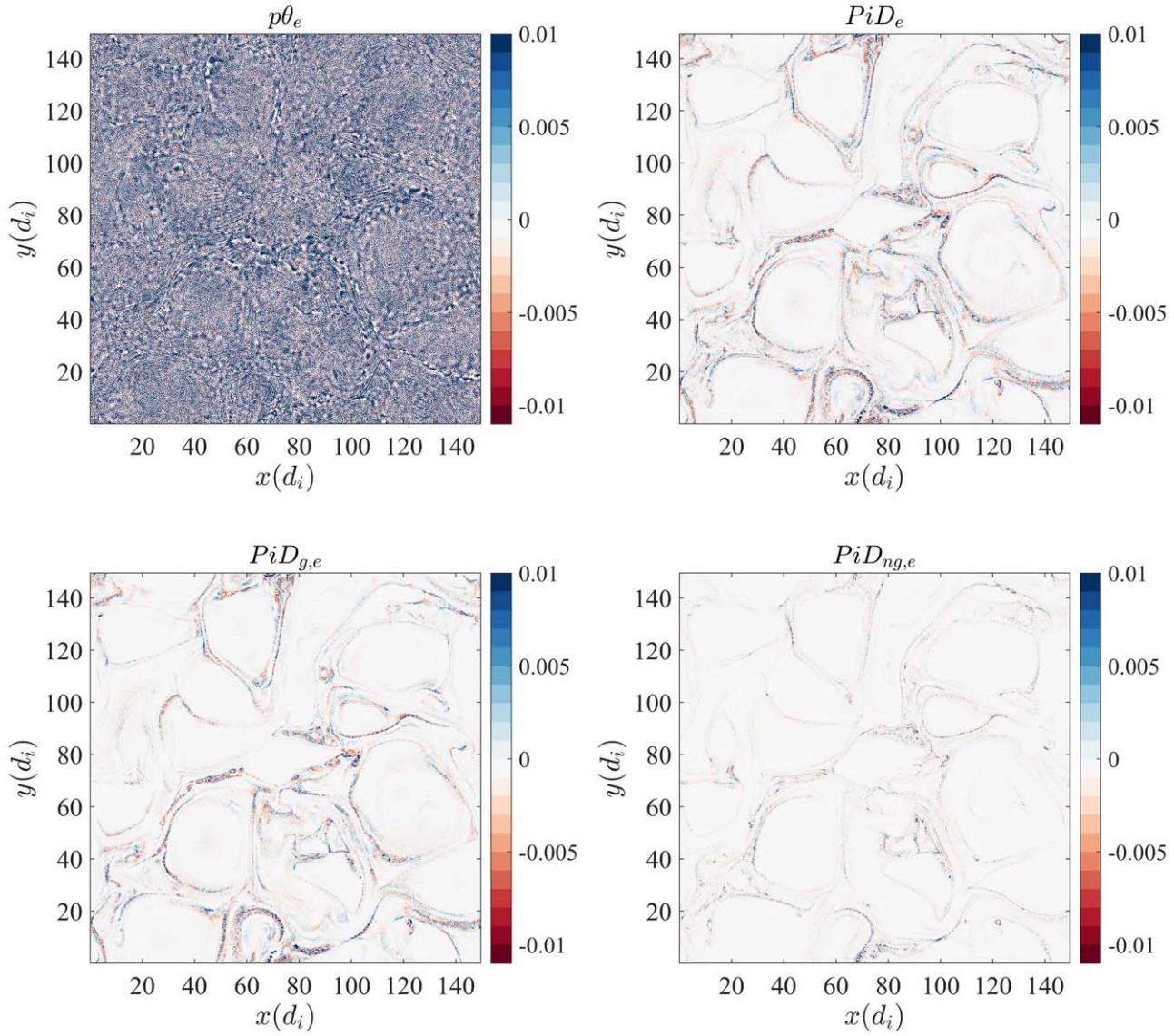

Figure 4. 2.5D PIC: contour maps of the incompressive and compressive parts and the gyrotropic and nongyrotropic parts of pressure–strain interaction for electrons at $\beta = 0.6$ and $t = 163\omega_{ci}^{-1}$. Only contour maps for electrons are shown and the patterns for protons are similar. The variables listed are in units of $m_i n_0 v_A^3 d_i^{-1}$.

and moreover, the small spacecraft separations were below the ion inertial length. These conditions enable reliable evaluation of the velocity strain tensor, employing techniques analogous to the curlometer technique (Dunlop et al. 2002). Several important values describing these intervals are reported in Table 2. Included are the proton plasma beta β_p, temporal mean values of the pressure–strain interaction PS_α, compressive $p\theta_\alpha$ versus incompressive PiD_α parts, and gyrotropic $PiD_{g,\alpha}$ versus nongyrotropic $PiD_{ng,\alpha}$ parts, given for each interval and for both electrons and protons. Note that the values for these intervals could be slightly different from those of Wang et al. (2021) due to the use of an improved algorithm.

Before we proceed with the MMS analysis, it is worth emphasizing how to interpret the simulation and observational results. Our simulations present several limitations and the magnetosheath turbulence shows much greater variability than that found in the numerical cases. Despite this great diversity of plasma turbulences, there are unifying features, such as energy-conversion processes. Therefore, the pressure–strain interaction, a measure of the local energy-conversion process, is fully general in both simulations and observations, but might exhibit different behaviors in varying turbulence systems.

Table 1
Description of One Selected Magnetosheath Interval of MMS on 2018 April 19 from 05:10:23 to 05:41:53 UTC

$\lvert\langle \boldsymbol{B}\rangle\rvert$(nT)	$\delta B/\lvert\langle \boldsymbol{B}\rangle\rvert$	$\langle n\rangle$(cm^{-3})	β_p	d_i(km)	L(km)
8.6	3.0	36.5	15.0	35.7	23

Note. $\lvert\langle \boldsymbol{B}\rangle\rvert$ is the mean magnetic field strength, $\delta B = \sqrt{\langle \lvert \boldsymbol{B}(t) - \langle \boldsymbol{B}\rangle\rvert^2\rangle}$ is the rms magnetic fluctuation, $\langle n\rangle$ is the mean plasma density, β_p is the proton plasma beta, d_i is the ion inertial length, and L indicates the mean separation between spacecraft

As done in the simulation analysis of Section 3, we can also investigate the local and global (averaged) properties of the pressure–strain interaction in the MMS magnetosheath observations. We start with the local properties and first make use of one long-burst interval from 05:10:23 to 05:41:53 UTC on 2018 April 19 as a reference, whose parameters are shown in

Table 1. The following results remain qualitatively unchanged for the other magnetosheath intervals in Table 2.

From Figures 5 and 6, we see similarities and differences between the observational results and the kinetic simulation results presented in Figures 3 and 4. First, in comparison with the incompressive part, the PDFs of the compressive parts for the electrons and protons have very extended tails in Figure 5, which indicate a local strong compression effect. Unlike the kinetic simulations, the temporal mean of the incompressive part is not dominant over the compressive part here, which we discuss in more detail later. Second, both the incompressive and compressive parts are bursty, but there exist very frequent oscillations with small magnitudes in the compressive part. Third, the PDF of the gyrotropic part for electrons has more extended tails than the nongyrotropic part in Figure 5, and vice versa for protons, as also seen in Figure 3 for the kinetic simulations.

Even though the local energy-conversion process quantified by the pressure–strain interaction is general in both the simulations and observations, caution is required when comparing global averages. Before we proceed with an MMS analysis similar to that of Figures 1 and 2, it is worth emphasizing the differences in handling PIC data and MMS data. (1) The time evolution of the thermal energy has been established for the simulations in Figure 1, but the corresponding analysis is not available for the in situ data, where it is not possible to follow the time evolution of an isolated plasma parcel. Lacking a direct way to compute the thermal energy increase over time, we resort to examination of the pressure–strain interaction related to the conversion of fluid kinetic energy into thermal energy, which is also supported by Pezzi et al. (2019), Yang et al. (2022), Bacchini et al. (2022), Roy et al. (2022). (2) According to Equations (1) and (2), in PIC simulations the spatial average over the entire periodic simulation domain represents precisely how much thermal energy is gained because all transport terms vanish exactly. So while the pointwise pressure–strain interaction in the simulations as shown in Figure 4 is not sign definite, its spatial average is positive definite since the net thermal energy is increasing and the net fluid kinetic energy is decreasing. However, in the MMS data the interval size is generally selected arbitrarily based on available Scientist-in-the-Loop (SITL) selections, and transport terms are likely to exert a significant influence on the temporal average over the whole interval of the pressure–strain interaction. So the temporal averages shown in Table 2 can be positive or negative. Therefore, instead of averaging over the whole interval, a useful compromise is to select subintervals with positive PS_α for both electrons and protons within each long interval. These subintervals definitely favor heating. In the following, the brackets $\langle\cdots\rangle$ denote the average over subintervals with positive PS_α within each long interval, which we call the regional average.

Figure 7 shows the ratio between the electron and proton regional averages of the pressure–strain interaction for the selected MMS data sets. In most cases, the ratio is larger than 1, which supports a stronger heating rate of protons compared to that of electrons. Unlike the clear correlation between the partitioning heating of protons and electrons and the plasma β for the kinetic simulations in Figure 1, there is only a fuzzy trend for protons gaining more thermal energy through PS_p with increasing β. We expect that a clearer determination of a net trend will require a large data sample, and we will attempt this in a subsequent study.

Further examination of the components of the pressure–strain interaction is shown in Figure 8. One striking feature is the relative prominence of the compressive part $\langle p\theta_\alpha\rangle$ over the incompressive part $\langle \mathrm{PiD}_\alpha\rangle$ for both electrons and ions. This result contrasts with the previously shown kinetic simulation result that features the dominance of the incompressive part. This is not so surprising when we recall that the magnetosheath is strongly influenced by proximity to the bow shock and the impinging solar wind and is thus, in general, more compressed. The kinetic simulations used here are weakly compressible and are obviously not intended to reproduce the compression feature of the magnetosheath. In spite of these contrasts, the observational results for agyrotropy are consistent with the simulation results; that is, gyrotropic heating dominates for electrons and the nongyrotropic heating is stronger for protons.

5. Conclusion and Discussion

Employing kinetic simulations and MMS observations, we have distinguished between compressive and incompressive heating channels, and between gyrotropic and nongyrotropic heating for electrons and protons. The conversion of energy into thermal energy (i.e., heating) is quantified by the pressure–strain interaction (Yang et al. 2017a). A direct comparison between the statistics obtained from the kinetic simulations and from the MMS observations in the Earth's magnetosheath shows an interesting agreement with regards to agyrotropy, while more significant differences are apparent in the decomposition into compressive versus incompressive parts.

We find that the gyrotropic part of the pressure–strain interaction is the dominant channel for electrons, while the nongyrotropic part contributes more for ions. Interestingly, our kinetic simulations suggest prominent incompressive heating, while the compressive part, as expected, dominates for the MMS observations in the magnetosheath, which is in general more compressed, driven by the impinging solar wind. These findings are quantified in Figure 9 where the ratios are averaged over the different values of plasma β that were sampled. Due to the significant differences between the simulations and observations, their comparison should be regarded as complementary rather than equivalent. For example, the magnetosheath is continuously driven, inhomogeneous, and open while the simulations in 2D geometry are decaying, homogeneous, and closed.

The results presented here may be expected to provide valuable guidance for tracking down specific processes that contribute to dissipation in collisionless plasmas. For example, Perri et al. (2020) found that the agyrotropy of the ion pressure tensor is moderately correlated with the deviation of the ion VDF from Maxwellian. There has been some success in attempts to investigate possible mechanisms of the generation of pressure tensor anisotropy in a fluid framework (Del Sarto et al. 2016; Del Sarto & Pegoraro 2018), where the pressure anisotropy is strongly correlated to the fluid strain. It is not a trivial challenge to find a closure model for the nongyrotropic part of the pressure tensor in collisionless plasma, as is readily accomplished in collisional MHD. Further work is needed on this path to provide a fuller understanding of dissipation in low collisionality plasma in space and elsewhere.

In most treatises on turbulence theory, there is a particular leaning toward the use of incompressible models due to their

Table 2
Magnetosheath Intervals of MMS

Date	$\langle n\rangle(\mathrm{cm}^{-3})$	β_p	α	PS_α	$p\theta_\alpha$	PiD_α	$\mathrm{PiD}_{g,\alpha}$	$\mathrm{PiD}_{ng,\alpha}$
2016 Jan 11	57.7	6.9	e	3.1×10^{-11}	3.0×10^{-11}	1.8×10^{-12}	2.3×10^{-12}	-4.9×10^{-13}
00:57:04-01:00:34			p	3.4×10^{-12}	-1.9×10^{-11}	2.3×10^{-11}	8.8×10^{-12}	1.4×10^{-11}
2016 Jan 24	34.7	12.0	e	2.2×10^{-12}	2.6×10^{-12}	-3.3×10^{-13}	4.3×10^{-13}	-7.5×10^{-13}
23:36:14-23:47:34			p	-4.5×10^{-11}	-4.8×10^{-11}	2.9×10^{-12}	1.1×10^{-12}	1.8×10^{-12}
2016 Dec 11	20.4	12.8	e	-8.3×10^{-10}	-8.3×10^{-10}	7.0×10^{-13}	-4.5×10^{-12}	5.2×10^{-12}
15:20:14-15:32:34			p	2.5×10^{-10}	2.6×10^{-10}	-5.6×10^{-12}	-3.4×10^{-12}	-2.1×10^{-12}
2016 Dec 18	35.7	5.5	e	-4.0×10^{-10}	-4.1×10^{-10}	2.9×10^{-12}	1.5×10^{-12}	1.4×10^{-12}
07:08:34-07:18:14			p	1.2×10^{-10}	1.1×10^{-10}	1.3×10^{-11}	5.3×10^{-12}	7.6×10^{-12}
2017 Jan 18	165.4	13.1	e	5.9×10^{-11}	7.2×10^{-11}	-1.3×10^{-11}	-8.5×10^{-12}	-4.2×10^{-12}
00:45:53-00:49:42			p	-4.4×10^{-10}	-4.3×10^{-10}	-8.4×10^{-12}	-5.1×10^{-12}	-3.3×10^{-12}
2017 Jan 27	14.7	9.3	e	2.3×10^{-10}	2.4×10^{-10}	-5.9×10^{-12}	-4.6×10^{-12}	-1.3×10^{-12}
08:02:03-08:08:03			p	-2.4×10^{-10}	-2.3×10^{-10}	-1.3×10^{-11}	-6.6×10^{-12}	-6.0×10^{-12}
2017 Sep 28	23.7	5.9	e	7.8×10^{-12}	1.1×10^{-11}	-2.8×10^{-12}	-2.9×10^{-12}	1.2×10^{-13}
06:31:33-07:01:43			p	-8.0×10^{-11}	-8.3×10^{-11}	3.1×10^{-12}	-2.6×10^{-13}	3.3×10^{-12}
2017 Oct 15	9.9	3.9	e	-2.1×10^{-11}	-2.2×10^{-11}	6.3×10^{-13}	5.8×10^{-13}	4.6×10^{-14}
22:23:43-22:26:43			p	7.0×10^{-12}	7.1×10^{-12}	-1.3×10^{-13}	3.1×10^{-12}	-3.2×10^{-12}
2017 Oct 30	17.1	14.4	e	3.1×10^{-12}	3.1×10^{-12}	-1.5×10^{-14}	-5.1×10^{-15}	-1.0×10^{-14}
18:57:23-19:01:13			p	1.7×10^{-11}	1.6×10^{-11}	7.8×10^{-13}	2.4×10^{-13}	5.4×10^{-13}
2017 Nov 10	8.0	9.8	e	-3.9×10^{-12}	-3.9×10^{-12}	-5.4×10^{-14}	2.5×10^{-14}	-9.2×10^{-14}
22:04:43-22:15:33			p	-1.0×10^{-11}	-7.1×10^{-12}	-3.0×10^{-12}	6.7×10^{-13}	-3.7×10^{-12}
2017 Nov 10	8.9	8.3	e	5.5×10^{-12}	5.5×10^{-12}	-3.6×10^{-15}	1.3×10^{-13}	-1.3×10^{-13}
22:35:43-22:52:03			p	4.1×10^{-11}	3.7×10^{-11}	3.9×10^{-12}	1.4×10^{-12}	2.5×10^{-12}
2017 Nov 22	14.3	16.0	e	-6.0×10^{-11}	-6.0×10^{-11}	-4.3×10^{-13}	-3.8×10^{-13}	-5.6×10^{-14}
07:43:43-07:47:23			p	2.4×10^{-11}	2.7×10^{-11}	-3.0×10^{-12}	-2.5×10^{-12}	-4.9×10^{-13}
2017 Nov 23	22.1	9.0	e	-1.3×10^{-10}	-1.3×10^{-10}	-1.3×10^{-13}	-5.8×10^{-14}	-7.5×10^{-14}
03:57:43-04:01:03			p	-3.8×10^{-11}	-4.4×10^{-11}	6.2×10^{-12}	3.6×10^{-12}	2.7×10^{-12}
2017 Nov 30	14.6	7.2	e	-6.0×10^{-11}	-6.0×10^{-11}	1.6×10^{-13}	1.9×10^{-13}	-2.6×10^{-14}
17:48:53-17:52:53			p	-2.7×10^{-11}	-2.7×10^{-11}	2.4×10^{-13}	4.5×10^{-13}	-2.1×10^{-13}
2017 Dec 6	10.2	4.7	e	-5.2×10^{-12}	-2.7×10^{-12}	-2.5×10^{-12}	-2.6×10^{-12}	6.3×10^{-14}
11:06:03-11:12:43			p	3.7×10^{-11}	3.6×10^{-11}	1.1×10^{-12}	2.1×10^{-12}	-1.0×10^{-12}
2017 Dec 21	28.1	8.9	e	-1.0×10^{-11}	-1.0×10^{-11}	-1.0×10^{-13}	-5.7×10^{-14}	-4.6×10^{-14}
06:41:55-07:03:51			p	2.2×10^{-12}	-1.3×10^{-12}	3.6×10^{-12}	1.6×10^{-12}	2.0×10^{-12}
2017 Dec 21	20.7	4.7	e	1.8×10^{-12}	1.8×10^{-12}	-4.8×10^{-14}	-3.4×10^{-14}	-1.4×10^{-14}
07:21:54-07:48:01			p	1.5×10^{-11}	1.3×10^{-11}	2.2×10^{-12}	1.9×10^{-12}	3.3×10^{-13}
2017 Dec 24	63.1	5.1	e	-7.0×10^{-11}	-7.0×10^{-11}	2.7×10^{-13}	6.5×10^{-13}	-3.8×10^{-13}
01:22:33-01:38:33			p	4.9×10^{-11}	3.5×10^{-11}	1.4×10^{-11}	5.4×10^{-12}	8.2×10^{-12}
2017 Dec 26	24.9	4.5	e	-2.0×10^{-12}	-2.3×10^{-13}	-1.8×10^{-12}	-1.8×10^{-12}	-2.7×10^{-14}
06:12:43-06:52:23			p	-4.5×10^{-12}	-7.1×10^{-12}	2.6×10^{-12}	1.1×10^{-12}	1.5×10^{-12}
2018 Jan 4	26.9	8.7	e	1.9×10^{-10}	1.9×10^{-10}	1.2×10^{-12}	1.1×10^{-12}	4.9×10^{-14}

Table 2
(Continued)

Date	$\langle n\rangle$(cm^{-3})	β_p	α	PS$_\alpha$	$p\theta_\alpha$	PiD$_\alpha$	PiD$_{g,\alpha}$	PiD$_{ng,\alpha}$
08:09:03-08:15:13			p	-1.3×10^{-11}	-1.3×10^{-11}	-9.4×10^{-13}	-8.9×10^{-13}	-5.2×10^{-14}
2018 Jan 21	36.7	8.7	e	2.0×10^{-10}	2.0×10^{-10}	4.0×10^{-12}	3.9×10^{-12}	1.3×10^{-13}
06:50:53- 06:56:33			p	1.4×10^{-10}	1.3×10^{-10}	1.3×10^{-11}	6.7×10^{-12}	6.8×10^{-12}
2018 Jan 26	41.8	10.7	e	5.8×10^{-10}	5.8×10^{-10}	-6.0×10^{-13}	-5.3×10^{-13}	-7.8×10^{-14}
09:24:13-09:31:03			p	-8.7×10^{-11}	-8.8×10^{-11}	1.7×10^{-12}	3.6×10^{-12}	-2.0×10^{-12}
2018 Jan 26	44.3	10.7	e	6.5×10^{-10}	6.5×10^{-10}	6.0×10^{-13}	3.8×10^{-13}	2.2×10^{-13}
09:33:03-09:41:22			p	7.2×10^{-11}	6.9×10^{-11}	2.9×10^{-12}	1.9×10^{-12}	1.0×10^{-12}
2018 Feb 18	14.6	5.6	e	4.1×10^{-11}	4.2×10^{-11}	-1.2×10^{-13}	-4.7×10^{-13}	3.5×10^{-13}
12:52:43-13:02:53			p	7.1×10^{-12}	-5.0×10^{-13}	7.6×10^{-12}	2.9×10^{-12}	4.7×10^{-12}
2018 Feb 21	65.5	8.1	e	1.8×10^{-11}	1.7×10^{-11}	1.2×10^{-12}	9.8×10^{-13}	2.2×10^{-13}
07:48:53-08:01:43			p	9.2×10^{-11}	7.2×10^{-11}	2.0×10^{-11}	1.1×10^{-11}	9.7×10^{-12}
2018 Mar 1	25.4	16.4	e	1.1×10^{-11}	1.1×10^{-11}	2.1×10^{-14}	5.4×10^{-14}	-3.4×10^{-14}
20:19:23-20:27:43			p	1.8×10^{-11}	1.6×10^{-11}	2.3×10^{-12}	3.1×10^{-13}	2.0×10^{-12}
2018 Mar 4	155.3	11.8	e	-2.3×10^{-10}	-2.3×10^{-10}	-2.6×10^{-12}	-3.0×10^{-12}	3.7×10^{-13}
01:08:53-01:16:33			p	3.2×10^{-11}	2.3×10^{-11}	9.2×10^{-12}	8.0×10^{-12}	1.2×10^{-12}
2018 Mar 15	19.2	5.5	e	3.9×10^{-11}	3.8×10^{-11}	8.2×10^{-13}	7.7×10^{-13}	4.6×10^{-14}
21:25:43- 21:32:53			p	2.6×10^{-12}	3.6×10^{-12}	-1.0×10^{-12}	-1.3×10^{-12}	2.3×10^{-13}
2018 Apr 19	36.5	15.0	e	1.8×10^{-11}	1.8×10^{-11}	1.0×10^{-13}	1.1×10^{-13}	-4.2×10^{-15}
05:10:23-05:41:53			p	5.1×10^{-12}	3.8×10^{-12}	1.3×10^{-12}	1.8×10^{-13}	1.1×10^{-12}
2018 Apr 23	16.4	7.0	e	-2.5×10^{-11}	-2.5×10^{-11}	-2.3×10^{-13}	-2.8×10^{-13}	4.0×10^{-14}
07:50:14-08:33:41			p	4.7×10^{-12}	4.1×10^{-12}	6.0×10^{-13}	3.3×10^{-13}	2.7×10^{-13}

Note. Note that intervals with mean density >50 may be suspect due to possible FPI detection system saturation. Shown in the table are the mean plasma density $\langle n\rangle$, proton plasma beta β_p, temporal averages of the pressure–strain interaction PS$_\alpha$, and its compressive $p\theta_\alpha$, incompressive PiD$_\alpha$, gyrotropic PiD$_{g,\alpha}$, and nongyrotropic PiD$_{ng,\alpha}$ parts for electrons and protons in units of (Jm^{-3}s^{-1}).

analytical simplicity. However, the magnetosheath intervals studied here clearly violate the assumption of incompressibility, as they exhibit prominent compressive parts of the pressure–strain interaction. One must appeal to compressible models to understand this. More confirmation from other kinetic simulations with strong compression as well as other observations is called for in future studies.

In examining the nature of the PDFs of the components of the pressure–strain interaction, we immediately confront the issue of reversibility of energy conversion in collisionless plasma. The full PDF width includes large positive and large negative values, which correspond to transferred energy into and out of the thermal energy, respectively. These pointwise positive and negative values mostly cancel out and end up as a relatively small mean upon averaging.

The averaged quantities we computed can be interpreted as the net change of the thermal energy if the system is isolated. This is the case for the kinetic simulations with periodic boundary conditions used here. However, in observations, other factors present challenges in interpreting the pressure–strain interaction as the net change of thermal energy. For example, spatial transport can move energy between adjacent plasma parcels, thus modifying local values of the temperature. Quantifying the relevant energy transport effects is deferred to future work.

We wish to acknowledge NASA Heliospheric GI grant Nos. 80NSSC21K0739 and NASA grant No. 80NSSC21K1458 at Princeton University, NASA MMS Theory and Modeling team grant No. 80NSSC19K0565, LWS grant 80NSSC20K0198 at Delaware, and an NSF-DOE grant PHY2108834 at Delaware. All MMS data are available at https://lasp.colorado.edu/mms/sdc/.

Appendix
Magnetosheath Interval Details

All the intervals of MMS measurements in this paper are in Earth's magnetosheath, ranging from 2016 January to 2018 April. Intervals after 2018 June have been discarded due to the lack of electron moments from MMS4, which is required to compute the pressure–strain interaction for electrons. These intervals listed in Table 2 are also used by Wang et al. (2021). The mean values of the pressure–strain interaction in Table 2 are slightly different from those of Wang et al. (2021) due to the use of an improved algorithm.

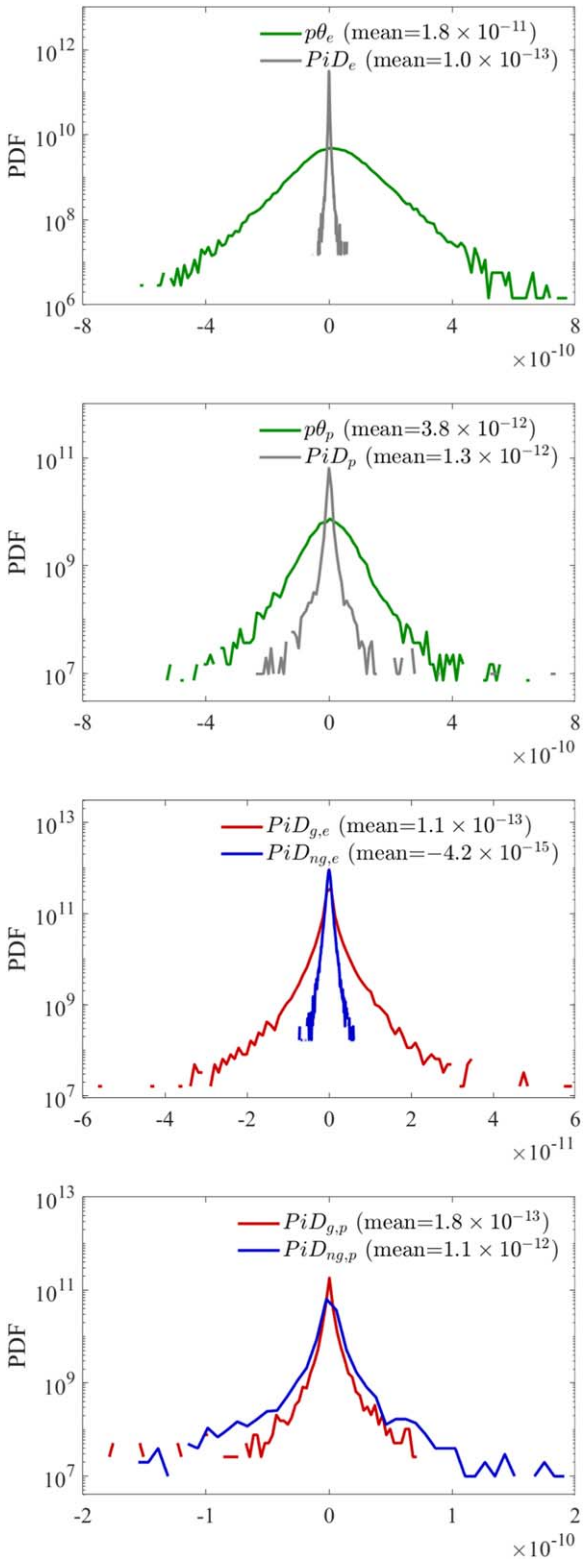

Figure 5. MMS: PDFs of the incompressive and compressive parts and the gyrotropic and nongyrotropic parts of the pressure–strain interaction for electrons and protons in units of (J m^{-3} s^{-1}). The magnetosheath interval on 2018 April 19 from 05:10:23 to 05:41:53 UTC is shown.

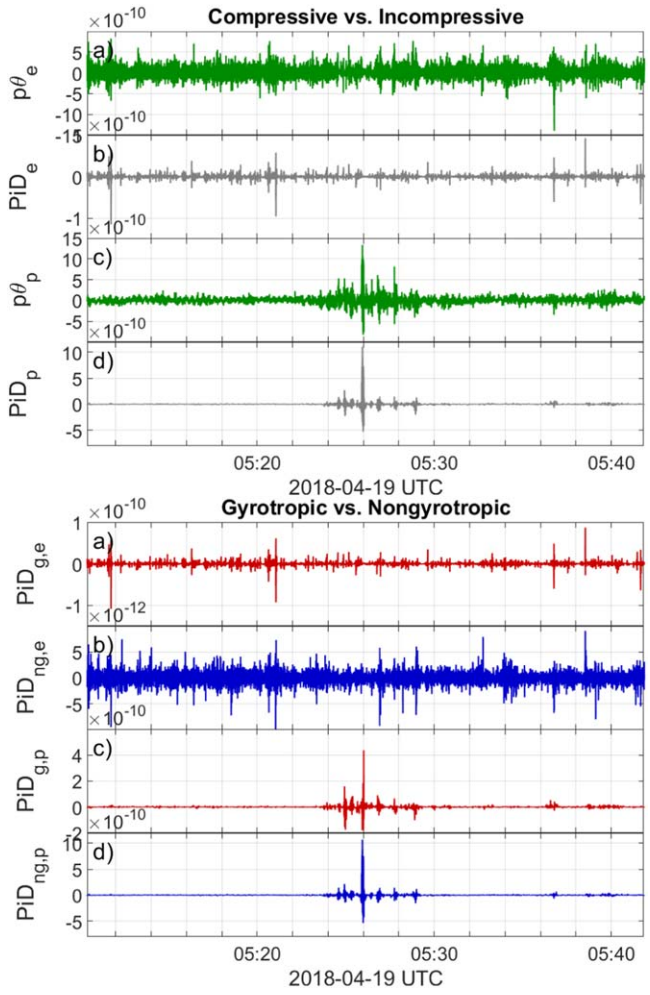

Figure 6. MMS: incompressive vs. compressive parts and gyrotropic vs. nongyrotropic parts of the pressure–strain interaction for electrons and protons in units of (J m^{-3} s^{-1}). The magnetosheath interval on 2018 April 19 from 05:10:23 to 05:41:53 UTC is shown.

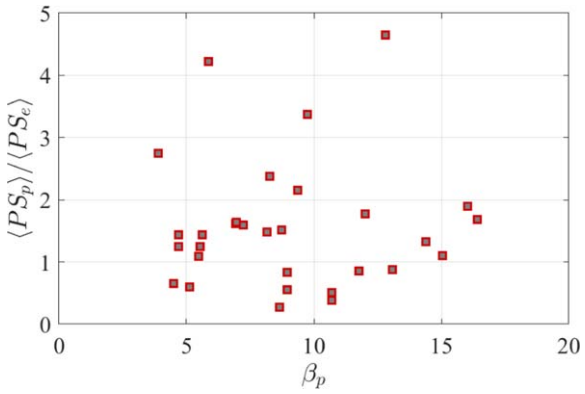

Figure 7. MMS: the ratio between the electron and proton regional averaged pressure–strain interaction at different βs. Here the regional average is taken over subintervals with both positive PS_e and PS_p in each long interval.

ORCID iDs

Yan Yang https://orcid.org/0000-0003-2965-7906
Francesco Pecora https://orcid.org/0000-0003-4168-590X
William H. Matthaeus https://orcid.org/0000-0001-7224-6024
Manuel Enrique Cuesta https://orcid.org/0000-0002-7341-2992
Alexandros Chasapis https://orcid.org/0000-0001-8478-5797

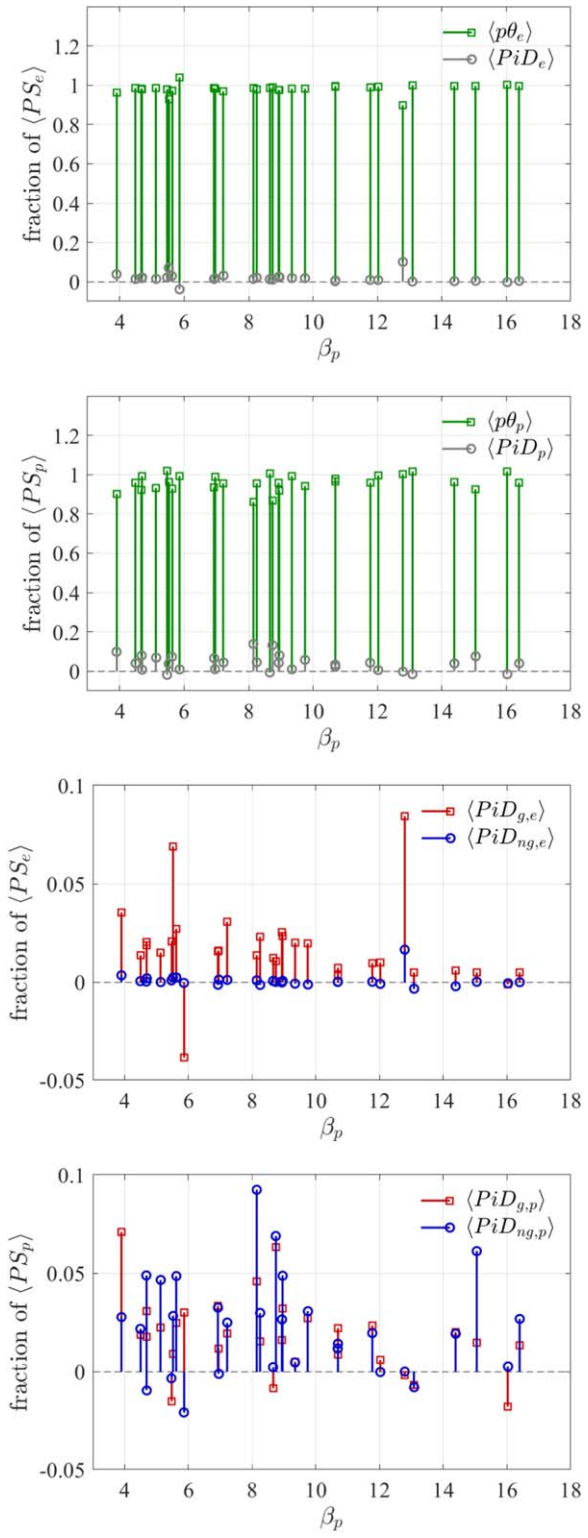

Figure 8. MMS: percentages of the regional averaged compressive $\langle p\theta_\alpha \rangle$, incompressive $\langle \mathrm{PiD}_\alpha \rangle$, gyrotropic $\langle \mathrm{PiD}_{g,\alpha} \rangle$, and nongyrotropic $\langle \mathrm{PiD}_{ng,\alpha} \rangle$ contributions relative to the pressure–strain interaction $\langle \mathrm{PS}_\alpha \rangle$ for electrons and protons at different βs.

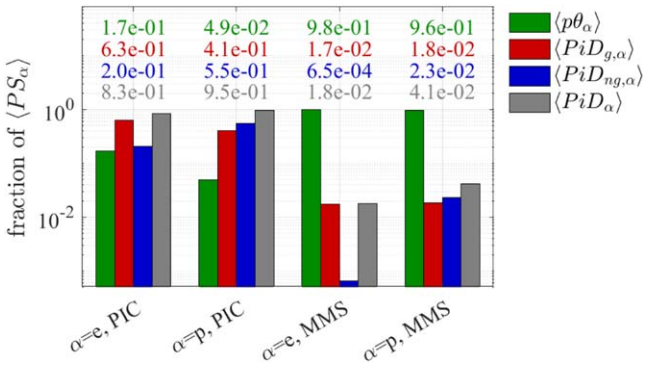

Figure 9. Percentages of the cumulatively time-integrated compressive $\langle p\theta_\alpha \rangle$, incompressive $\langle \mathrm{PiD}_\alpha \rangle$, gyrotropic $\langle \mathrm{PiD}_{g,\alpha} \rangle$, and nongyrotropic $\langle \mathrm{PiD}_{ng,\alpha} \rangle$ contributions relative to the pressure–strain interaction $\langle \mathrm{PS}_\alpha \rangle$ for electrons and protons averaged over different βs.

Tulasi Parashar https://orcid.org/0000-0003-0602-8381
Riddhi Bandyopadhyay https://orcid.org/0000-0002-6962-0959
D. J. Gershman https://orcid.org/0000-0003-1304-4769
J. L. Burch https://orcid.org/0000-0003-0452-8403

References

Adhikari, S., Parashar, T., Shay, M., et al. 2021, PhRvE, 104, 065206
Bacchini, F., Pucci, F., Malara, F., & Lapenta, G. 2022, PhRvL, 128, 025101
Bandyopadhyay, R., Chasapis, A., Matthaeus, W., et al. 2021, PhPl, 28, 112305
Barbhuiya, M. H., & Cassak, P. A. 2022, PhPl, 29, 122308
Braginskii, S. I. 1965, RvMPP, 1, 205
Burch, J. L., Moore, T. E., Torbert, R. B., & Giles, B. L. 2016, SSRv, 199, 5
Burch, J. L., Torbert, R. B., Phan, T. D., et al. 2016, Sci, 352, aaf2939
Cassak, P., Baylor, R., Fermo, R., et al. 2015, PhPl, 22, 020705
Cassak, P. A., & Barbhuiya, M. H. 2022, PhPl, 29, 122306
Cassak, P. A., Barbhuiya, M. H., & Weldon, H. A. 2022, PhPL, 29, 122307
Cerri, S. S., Henri, P., Califano, F., et al. 2013, PhPl, 20, 112112
Cerri, S. S., Pegoraro, F., Califano, F. D., & Del Sarto, J. F. 2014, PhPl, 21, 112109
Chapman, S., & Cowling, T. G. 1939, The Mathematical Theory of nonuniform Gases: an Account of the Kinetic Theory of Viscosity, Thermal Conduction and Diffusion in Gases (Cambridge: Cambridge Univ. Press)
Chasapis, A., Yang, Y., Matthaeus, W., et al. 2018, ApJ, 862, 32
Chew, G., Goldberger, M., & Low, F. 1956, RSPSA, 236, 112
Cranmer, S. R. 2009, LRSP, 6, 1
D. Del Sarto, Pegoraro, F., & Califano, F. 2016, PhRvE, 93, 053203
De Camillis, S., Cerri, S. S., Califano, F., & Pegoraro, F. 2016, PPCF, 58, 045007
Del Sarto, D., & Pegoraro, F. 2018, MNRAS, 475, 181
Du, S., Guo, F., Zank, G. P., Li, X., & Stanier, A. 2018, ApJ, 867, 16
Dunlop, M. W., Balogh, A., Glassmeier, K.-H., & Robert, P. 2002, JGRA, 107, 1384
Fadanelli, S., Lavraud, B., Califano, F., et al. 2021, JGRA, 126, e2020JA028333
Graham, D. B., Khotyaintsev, Y. V., Vaivads, A., et al. 2017, PhRvL, 119, 025101
Haggerty, C. C., Parashar, T. N., Matthaeus, W. H., et al. 2017, PhPl, 24, 102308
He, J., Wang, L., Tu, C., Marsch, E., & Zong, Q. 2015, ApJL, 800, L31
Hellinger, P., Montagud-Camps, V., Franci, L., et al. 2022, ApJ, 930, 48
Hesse, M., Kuznetsova, M., & Hoshino, M. 2002, GeoRL, 29, 4
Hesse, M., Schindler, K., Birn, J., & Kuznetsova, M. 1999, PhPl, 6, 1781
Howes, G. G. 2010, MNRAS, 409, L104
Hughes, R. S., Gary, S. P., & Wang, J. 2014, GeoRL, 41, 8681
Hughes, R. S., Gary, S. P., Wang, J., & Parashar, T. N. 2017, ApJL, 847, L14
Hunana, P., Tenerani, A., Zank, G., et al. 2019, JPlPh, 85, 205850602
Karimabadi, H., Roytershteyn, V., Wan, M., et al. 2013, PhPl, 20, 012303
Kaufman, A. N. 1960, PhFl, 3, 610
Kawazura, Y., Barnes, M., & Schekochihin, A. A. 2019, PNAS, 116, 771
Khanna, M., & Rajaram, R. 1982, JPlPh, 28, 459
Klein, K. G., Howes, G. G., & TenBarge, J. M. 2017, JPlPh, 83, 535830401
Landshoff, R. 1949, PhRv, 76, 904
Lapenta, G., El Alaoui, M., Berchem, J., & Walker, R. 2020, JGRA, 125, e2019JA027276
Marshall, W. 1960, The Kinetic Theory of an Ionized Gas, Vol. 2247 (Harwell: Atomic Energy Research Establishment)
Matthaeus, W. H., Parashar, T. N., Wan, M., & Wu, P. 2016, ApJL, 827, L7

Matthaeus, W. H., Yang, Y., Wan, M., et al. 2020, ApJ, 891, 101
Parashar, T. N., Matthaeus, W. H., & Shay, M. A. 2018, ApJL, 864, L21
Perri, S., Perrone, D., Yordanova, E., et al. 2020, JPlPh, 86, 905860108
Pezzi, O., Yang, Y., Valentini, F., et al. 2019, PhPl, 26, 072301
Pezzi, O., Liang, H., Juno, J., et al. 2020, MNRAS, 505, 4857
Pollock, C., Moore, T., Jacques, A., et al. 2016, ssr, 199, 331
Pritchett, P. 2001, JGRA, 106, 3783
Quataert, E. 1998, ApJ, 500, 978
Ricci, P., Brackbill, J., Daughton, W., & Lapenta, G. 2004, PhPl, 11, 4102
Roberts, K., & Taylor, J. 1962, PhRvL, 8, 197
Roy, S., Bandyopadhyay, R., Yang, Y., et al. 2022, ApJ, 941, 137
Rueda, J. A. A., Verscharen, D., Wicks, R. T., et al. 2022, ApJ, 938, 4
Russell, C. T., Anderson, B. J., Baumjohann, W., et al. 2016, SSRv, 199, 189
Schekochihin, A., Kawazura, Y., & Barnes, M. 2019, JPlPh, 85, 905850303
Scudder, J., & Daughton, W. 2008, JGRA, 113, A06222
Scudder, J., Holdaway, R., Daughton, W., et al. 2012, PhRvL, 108, 225005
Scudder, J., Karimabadi, H., Daughton, W., & Roytershteyn, V. 2015, PhPl, 22, 101204
Servidio, S., Osman, K., Valentini, F., et al. 2014, ApJL, 781, L27
Servidio, S., Valentini, F., Califano, F., & Veltri, P. 2012, PhRvL, 108, 045001
Servidio, S., Valentini, F., Perrone, D., et al. 2015, JPlPh, 81, 3207
Sitnov, M., Merkin, V., Roytershteyn, V., & Swisdak, M. 2018, GeoRL, 45, 4639
Smolyakov, A. 1998, CaJPh, 76, 321
Spitzer, L., Jr, & Härm, R. 1953, PhRv, 89, 977
Stawarz, J. E., Smith, C. W., Vasquez, B. J., Forman, M. A., & MacBride, B. T. 2009, ApJ, 697, 1119
Thompson, W. 1961, RPPh, 24, 363
Valentini, F., Servidio, S., Perrone, D., et al. 2014, PhPl, 21, 082307
Vasyliunas, V. 1975, RvGeo, 13, 303
Vech, D., Klein, K. G., & Kasper, J. C. 2017, ApJL, 850, L11
Wan, M., Matthaeus, W. H., Karimabadi, H., et al. 2012, PhRvL, 109, 195001
Wang, Y., Bandyopadhyay, R., Chhiber, R., et al. 2021, JGRA, 126, e29000
Wu, P., Wan, M., Matthaeus, W. H., Shay, M. A., & Swisdak, M. 2013, PhRvL, 111, 121105
Yajima, N. 1966, PThPh, 36, 1
Yang, Y., Matthaeus, W. H., Roy, S., et al. 2022, ApJ, 929, 142
Yang, Y., Wan, M., Matthaeus, W. H., et al. 2019, MNRAS, 482, 4933
Yang, Y., Matthaeus, W. H., Parashar, T. N., et al. 2017a, PhPl, 24, 072306
Yang, Y., Matthaeus, W. H., Parashar, T. N., et al. 2017b, PhRvE, 95, 061201
Zeiler, A., Biskamp, D., Drake, J. F., et al. 2002, JGR, 107, 1230
Zenitani, S., Hesse, M., Klimas, A., & Kuznetsova, M. 2011, PhRvL, 106, 195003
Zhou, M., Man, H., Yang, Y., Zhong, Z., & Deng, X. 2021, GeoRL, 48, e2021GL096372